Supplemental Information

# Decoupling Strategy

for Enhanced Syngas Generation

from Photoelectrochemical CO$_2$ Reduction

Sheng Chu, Pengfei Ou, Roksana Tonny Rashid, Pegah Ghamari, Renjie Wang, Hong Nhung Tran, Songrui Zhao, Huiyan Zhang, Jun Song, and Zetian Mi
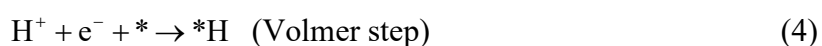
Transparent Methods

Density functional theory (DFT) calculations: DFT calculations were performed with BEEF-vdW (Wellendorff et al., 2012) exchange-correlation functional and projector augmented wave (PAW) pseudopotential (Blöchl, 1994; Kresse and Joubert, 1999) within the Vienna Ab-initio Simulation Package (VASP) (Kresse and Hafner, 1994; Kresse and Furthmüller, 1996). A cut-off energy of 400 eV was chosen, and structural optimization were achieved until the residual force on each atom was smaller than 0.01 eV Å^{-1}. A (3 × 3) and (3 × 1) surface unit with a four-layer slab were modeled for the (111) and (211) facets of fcc metals respectively, both containing 9 surface metal atoms per supercell. All slabs were spaced more than 20 Å perpendicular to the slab surface to avoid interaction due to their periodicity. A 4 × 4 × 1 Monkhorst-Pack mesh of k-points (Monkhorst and Pack, 1976) was used both for (111) and (211) facets. When relaxing the geometries, adsorbates and the top two layers were allowed to relax, while the bottom two layers were fixed to their initial bulk positions.
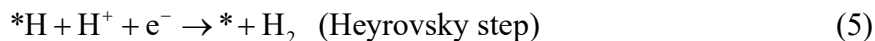
The reaction mechanism of CO_2 reduction to CO in an aqueous solution is suggested to include the following steps (Sheng et al., 2017):

$$CO_2 + H^+ + e^- + * \rightarrow {}^*COOH \tag{1}$$

$$^*COOH + H^+ + e^- \rightarrow {}^*CO + H_2O \tag{2}$$

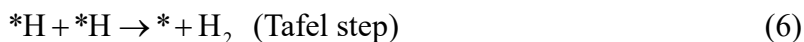$$^*CO \rightarrow {}^* + CO \tag{3}$$
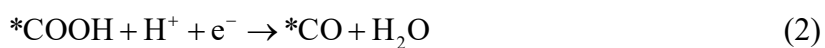
where * denotes either a surface-bound species or a vacant catalytic active site.

The HER consists of two consecutive proton-electron pair transfer steps:

$$H^+ + e^- + * \rightarrow {}^*H \quad \text{(Volmer step)} \tag{4}$$

$$*H + H^+ + e^- \rightarrow * + H_2 \quad \text{(Heyrovsky step)} \tag{5}$$

or

$$*H + *H \rightarrow * + H_2 \quad \text{(Tafel step)} \tag{6}$$

Free energy corrections for adsorbates and gas molecules: The CO_2RR and HER activity maps were calculated by computational hydrogen electrode (CHE) model suggested by Nørskov et al (Nørskov et al., 2004). By employing the CHE model, a proton/electron ($H^+ + e^-$) in solution can be directly treated and the effect of a bias can be applied by shifting by ΔG by +neU, where n is the number of proton-electron pairs transferred, e is the elementary positive charge, and U is the applied potential. The free energy change (ΔG) is calculated as $\Delta G = \Delta E + \Delta ZPE + \int C_p dT - T \Delta S$, where ΔE is the total energy directly obtained from DFT calculations, ΔZPE is the change in zero-point energy, C_p is the heat capacity, T is temperature, and ΔS is the change in entropy. The temperature is set to 298.15 K to compare current DFT results with the experimental data. The contributions to the free energy for each adsorbate involved in the lowest-energy pathways are listed in Table S1. As indicated in a previous study (Tripković et al., 2010), the reaction intermediates would be stabilized by the hexagonal water overlayer above them, therefore the solvation correction was also employed by applying a *COOH and *CO stabilization of 0.25 and 0.1 eV, respectively.

DFT calculations of non-adsorbed species were performed using the same techniques as described above for adsorbed species, except with a Fermi-level smearing of 0.01 eV. The components of the energy calculations for all non-adsorbed species are also listed in Table S1.

Sample synthesis: GaN nanowire arrays were grown on planar p-n Si wafer by plasma-assisted molecular beam epitaxy as previously described (Vanka et al., 2018). Au nanoparticles were deposited on GaN nanowires using an e-beam evaporator at a deposition rate of 0.1 Å/s for 500 s, followed with thermal annealing in Ar at 650 °C for 2 min. During the annealing process, small Au nanoparticles migrated and coalesced to form large Au nanoparticles on GaN nanowires for decreasing the surface energy (Sui et al., 2013). Au was favourable to grow on the c-plane of GaN nanowires as a tipped heterostructure. This can be explained by the smaller formation energy for Au on c-plane GaN, partly due to the smaller lattice mismatch between Au(111) and c-plane GaN compared to m-plane GaN (0.24, 0.26 and 0.28 nm, respectively) (Li et al., 2014). Prior to the Au e-beam deposition, the GaN nanowires on p-n Si substrate was pre-treated with concentrated HCl solution for 30 s to remove native oxide. Pt nanoparticles were deposited on GaN nanowires by photodeposition using H_2PtCl_6 (99.9%, Sigma Aldrich) as precursor from an aqueous methanol solution (15 mL methanol and 60 mL deionized water). 2, 5 and 12 μL of 0.2 M H_2PtCl_6 were used for the preparation of $AuPt_{0.1}/GaN/n^+$-p Si, $AuPt_{0.2}/GaN/n^+$-p Si and $AuPt_{0.4}/GaN/n^+$-p Si, respectivily. $NiFeO_x/BiVO_4$ photoanode was prepared according to a previously reported method (Kim and Choi, 2014; Kobayashi et al., 2018).

Characterization: ICP-AES analyses were performed on a Thermo Scientific iCAP 6000 Series inductively coupled plasma–atomic emission spectroscopy instrument to determine the loading amount of metal cocatalysts. The samples were digested in aqua regia (HNO_3:HCl=1:3) at 95 °C for 3 h before the analysis. The morphology of samples was characterized by SEM and TEM. SEM images were acquired from an Inspect F-50 FE-SEM system at an accelerating

voltage of 5 keV. TEM images were attained on FEI Tecnai G2 F20 microscope at 200 keV, with EDX attached. The nanowires were scratched off from the Si substrate onto a Cu TEM grid. Surface chemical compositions of samples were analyzed by XPS in a Thermo Scientific K-Alpha XPS system with a monochromatic Al Kα source (hv = 1486.6 eV). The binding energies were calibrated using the C1s peak at 284.8 eV as the reference.

PEC measurements: PEC CO_2 reduction was performed in a three-electrode configuration with $AuPt_x$/GaN/n^+-p Si as the working electrode, Pt wire as the counter electrode and Ag/AgCl as the reference electrode. The gastight PEC reactor has three compartments, including working compartment, reference compartment, and counter compartment. The compartments were separated by proton exchange membranes. Prior to PEC CO_2 reduction experiments, 40 mL electrolyte of 0.5 M $KHCO_3$ was added into the cell and purged with CO_2 for 30 min, resulting in electrolyte pH at 7.5. The light source was a solar simulator (Newport Oriel LCS-100) with a calibrated light intensity of 100 mW cm^{-2} (1 sun) on the sample surface. The PEC data were collected by a potentiostat (Gamry Instruments, Interface 1000). The *J-V* curve was obtained at a scan rate of 20 mV/s. Chronoamperometry for product analysis was performed at a certain potential for 100 min. Gas products after the photoelectrolysis were analysed by a gas chromatograph (Shimadzu GC-8A) with a thermal conductivity detector for H_2 concentration, and a gas chromatograph (Shimadzu GC-2014) with a flame ionization detector for CO and hydrocarbons concentration. Each measurement was performed several times to check the consistency of experiments. The average values out of the multiple measurements were presented and error bars denote one standard deviation.

The applied bias photon-to-current efficiency (ABPE) was calculated using the following equation:

$$\text{ABPE}(\%) = \left[\frac{J(\text{mA·cm}^{-2})\times\text{FE}_{\text{CO}}(\%)\times(1.34-V_{\text{bias}})(V)+J(\text{mA·cm}^{-2})\times\text{FE}_{\text{H}_2}(\%)\times(1.23-V_{\text{bias}})(V)}{P_{\text{in}}(\text{mW·cm}^{-2})}\right]$$

(7)

where J is the photocurrent density, FE_{CO} and FE_{H_2} are faradaic efficiency to produce CO and H_2 respectively, V_{bias} is the applied potential versus an ideal counter electrode for O_2 evolution (+1.23 V vs. RHE), and P_{in} is the light intensity (100 mW cm^{-2}).

The unassisted overall solar-to-syngas (STS) efficiency η_{STS} was calculated using the following equation:

$$\eta_{\text{STS}}(\%) = \left[\frac{J(\text{mA}\cdot\text{cm}^{-2})\times\text{FE}_{\text{CO}}(\%)\times1.34(V)+J(\text{mA}\cdot\text{cm}^{-2})\times\text{FE}_{H_2}(\%)\times1.23(V)}{P_{\text{in}}(\text{mW}\cdot\text{cm}^{-2})}\right]$$

(8)

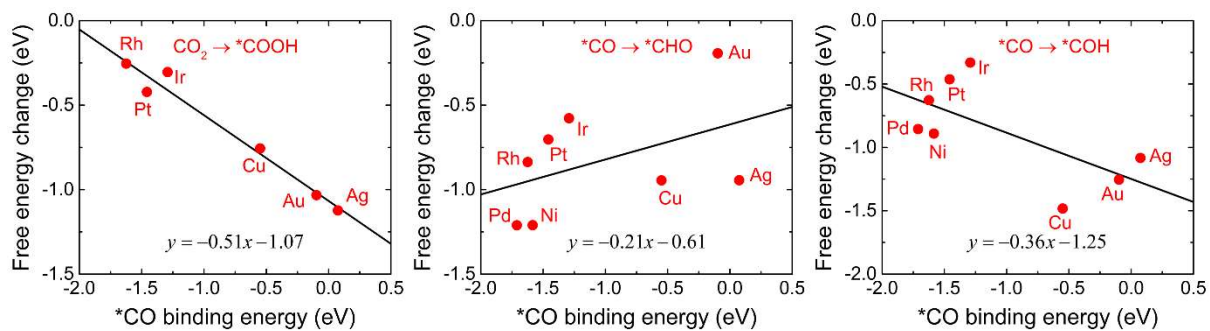where J is the unbiased photocurrent density measured in a two-electrode cell.

Figure S1. Scaling relations between the *CO binding energy and basic reactions in CO_2RR on transition metal fcc(111) facet. The fitted equations are shown in the insets. Related to Figure 1.
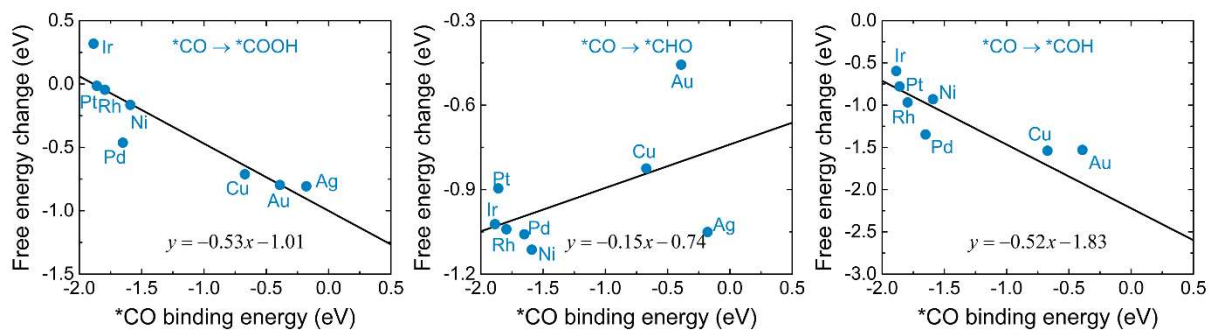
Figure S2. Scaling relations between the *CO binding energy and basic reactions in CO$_2$RR on transition metal fcc(211) facet. The fitted equations are shown in the insets. Related to Figure 1.
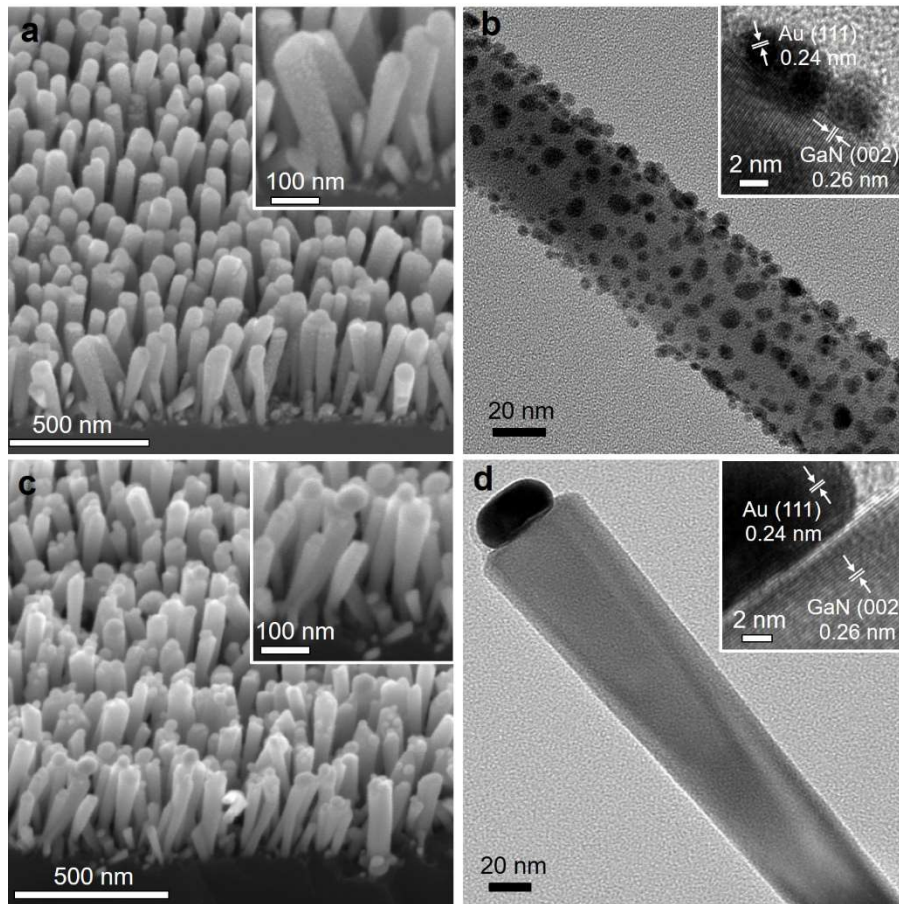
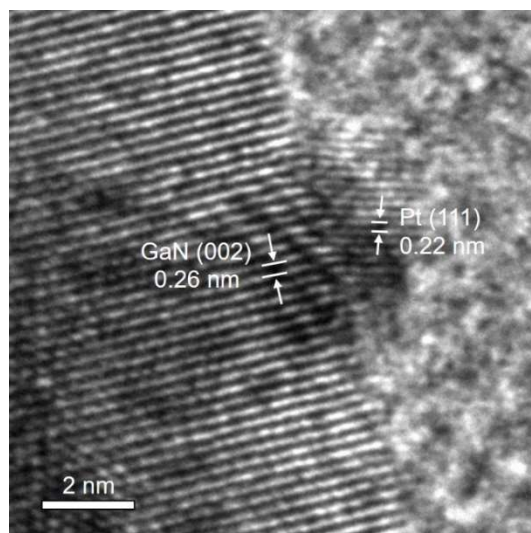**Figure S3.** SEM and TEM images of Au/GaN/n$^+$-p Si before (a, b) and after (c, d) annealing process. Related to Figure 2.

Figure S4. High-resolution TEM image of Pt nanoparticle on GaN nanowire. Related to Figure 2.
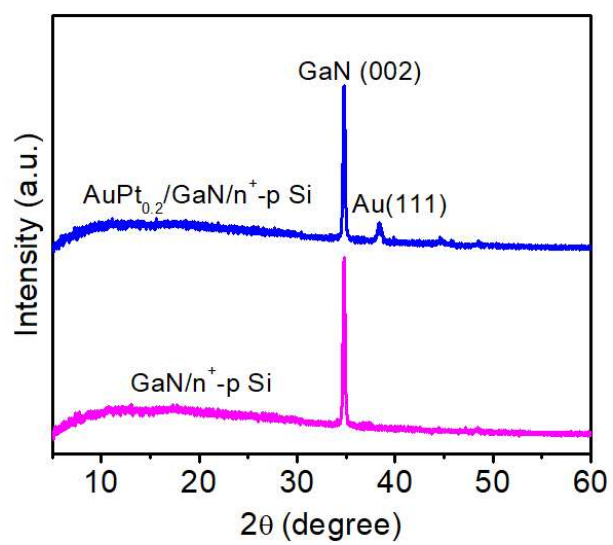
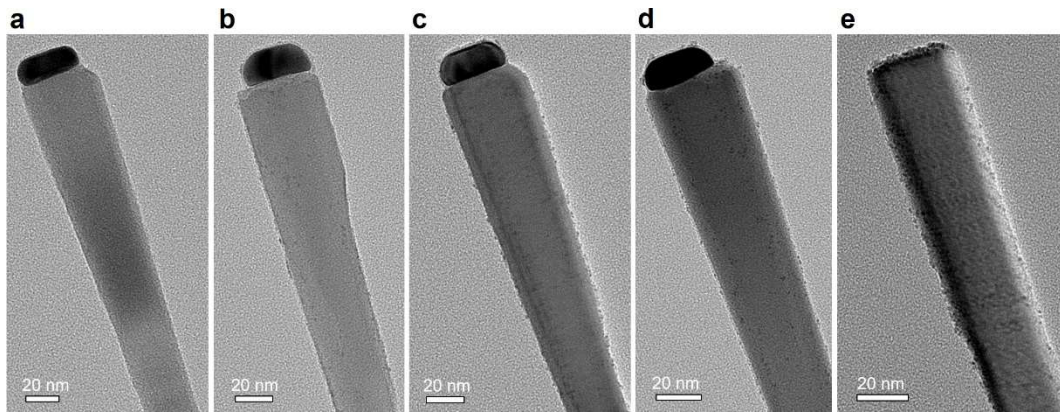**Figure S5.** XRD patterns of GaN/n^+-p Si and AuPt$_{0.2}$/GaN/n^+-p Si. Related to Figure 2.

Figure S6. TEM images of (a) Au/GaN/n^+-p Si, (b) AuPt$_{0.1}$/GaN/n^+-p Si, (c) AuPt$_{0.2}$/GaN/n^+-p Si, (d) AuPt$_{0.4}$/GaN/n^+-p Si and (e) Pt/GaN/n^+-p Si. Related to Figure 2.
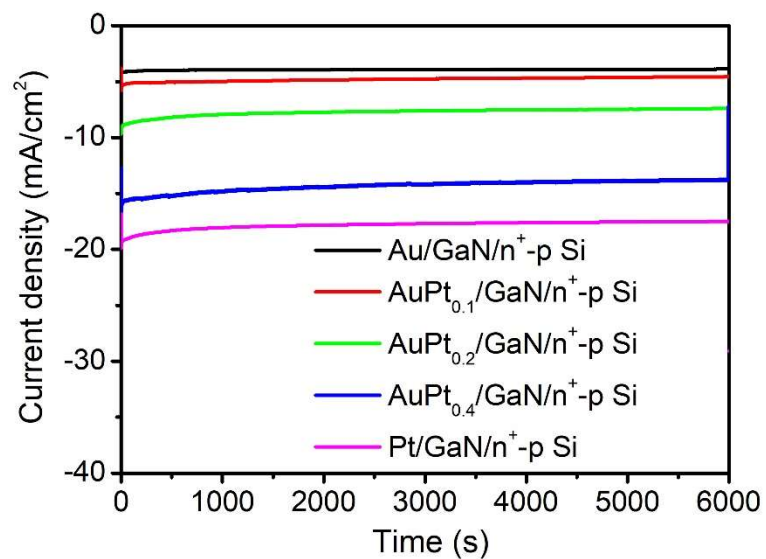
Figure S7. Chronoamperometry data of $AuPt_x/GaN/n^+$-p Si photocathodes at +0.17 V vs RHE in CO_2-saturated 0.5 M $KHCO_3$ (pH 7.5) under AM 1.5G one-sun illumination. Related to Figure 3.
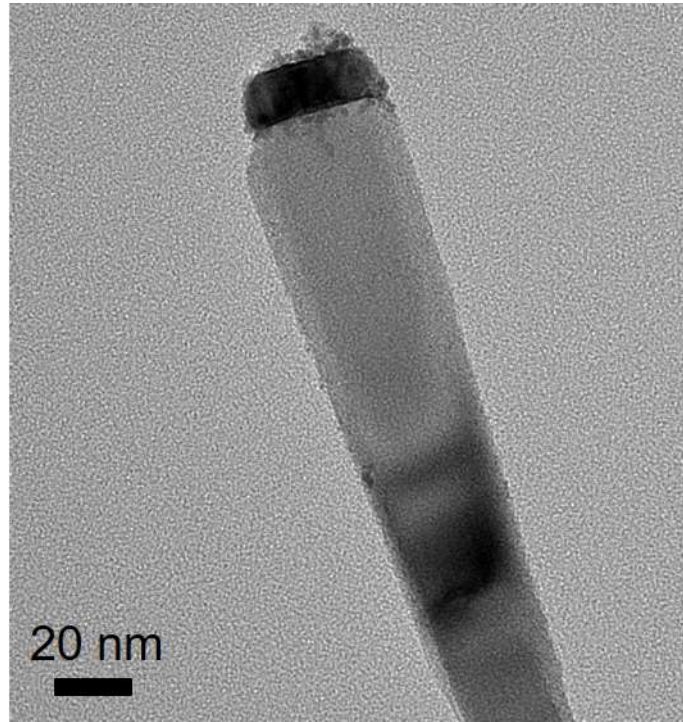
Figure S8. TEM image of $AuPt_{0.1}/GaN/n^+$-p Si using $Pt(NH_3)_4Cl_2$ as Pt precursor. Related to Figure 3.
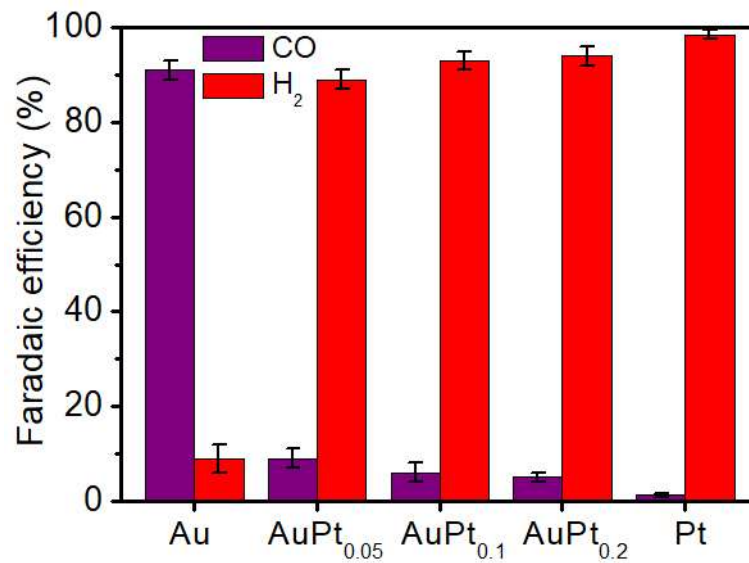
Figure S9. FEs for CO (purple bars) and H_2 (red bars) of $AuPt_x/GaN/n^+$-p Si with different cocatalyst compositions at +0.17 V vs RHE using $Pt(NH_3)_4Cl_2$ as Pt precursor. Error bars represent one standard deviation of multiple independent measurements. Related to Figure 3.
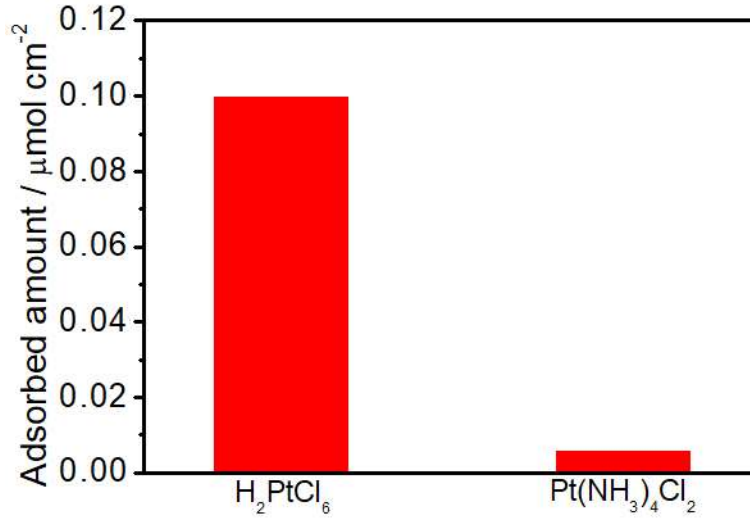
Figure S10. The adsorption amount of Pt precursor on Au/GaN/n^+-p Si sample. 3 cm^2 of wafer sample was immersed in 50 mL H$_2$PtCl$_6$ or Pt(NH$_3$)$_4$Cl$_2$ aqueous solution (0.01 mmol/L) overnight. The Pt concentration in the solution was analyzed by ICP-AES, and the adsorbed Pt amount was calculated. The results show the stronger adsorption of PtCl$_6^{2-}$ than that of Pt(NH$_3$)$_4^{2+}$. Related to Figure 3.
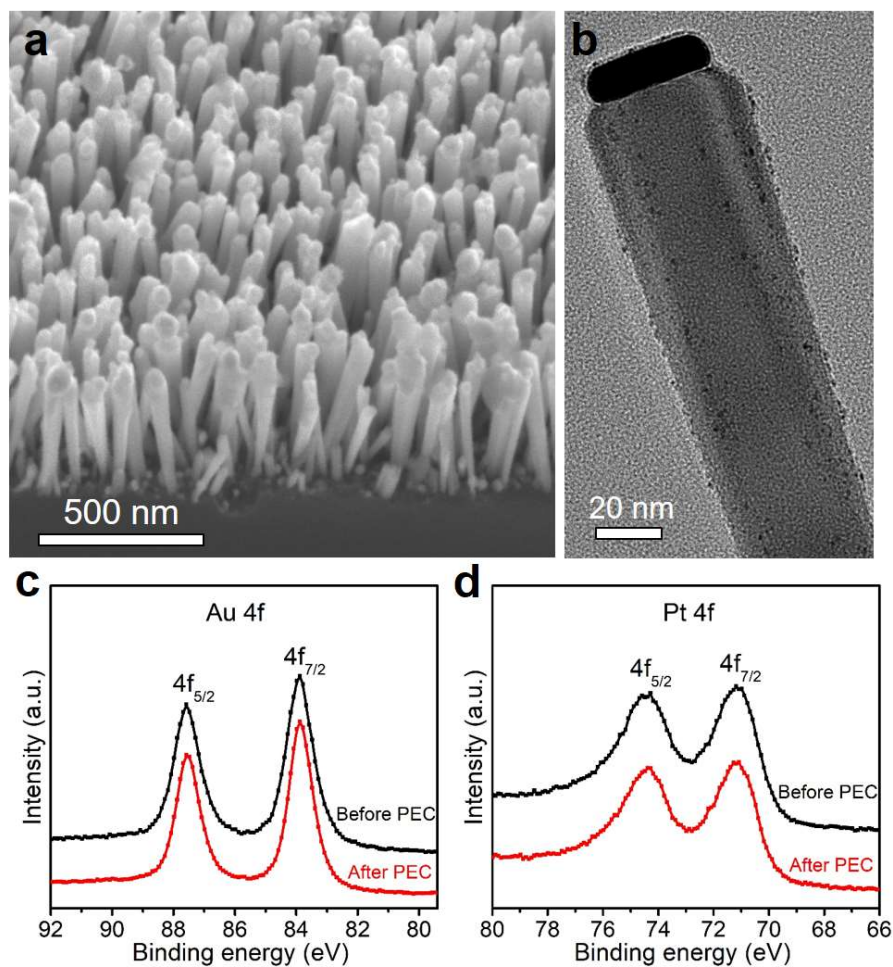
Figure S11. (a) SEM and (b) TEM images of $AuPt_{0.2}/GaN/n^+$-p Si photocathode after PEC stability test. XPS analysis of (c) Au 4f and (d) Pt 4f of $AuPt_{0.2}/GaN/n^+$-p Si photocathode before and after PEC stability test. Related to Figure 3.
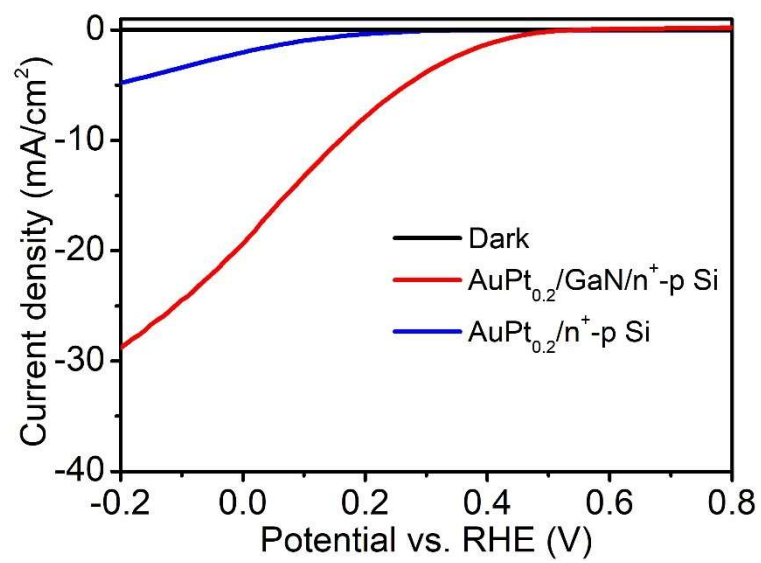
Figure S12. *J-V* curves of $AuPt_{0.2}/n^+$-p Si and $AuPt_{0.2}/GaN/n^+$-p Si. Related to Figure 3.
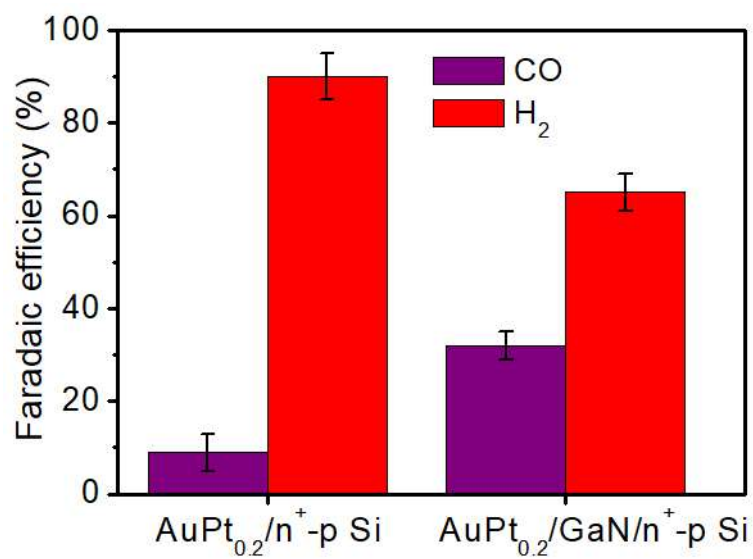
Figure S13. FEs for CO (purple bars) and H_2 (red bars) of $AuPt_{0.2}/n^+$-p Si and $AuPt_{0.2}/GaN/n^+$-p Si at +0.17 V vs RHE. The low FE for CO on $AuPt_{0.2}/n^+$-p Si might be ascribed to the close proximity of Au and Pt cocatalysts when they deposited on planar Si substrate. Error bars represent one standard deviation of multiple independent measurements. Related to Figure 3.
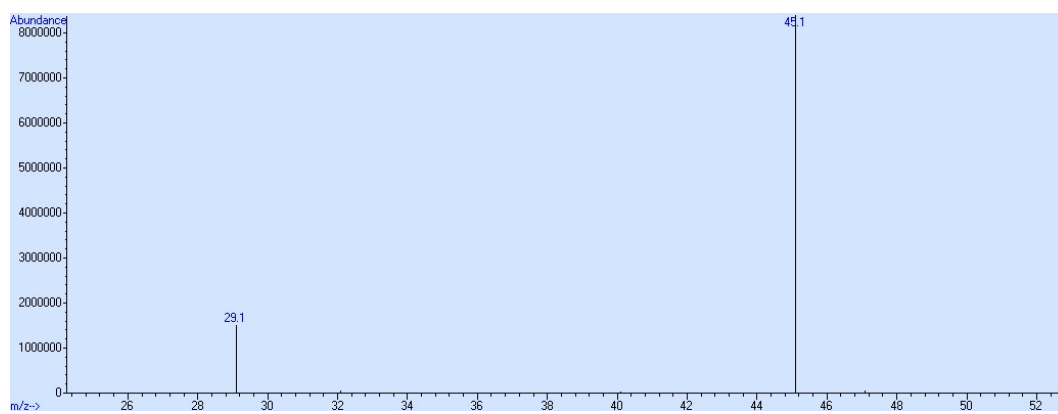
Figure S14. Mass spectrometry chromatogram of the gas phase analysis after ^{13}C-labeled isotope experiment. Related to Figure 3.
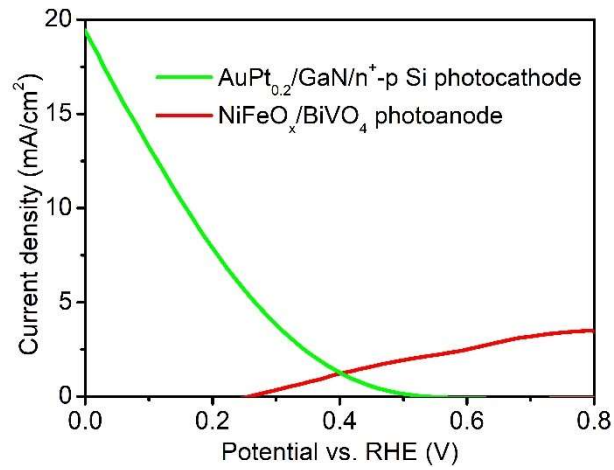
Figure S15. *J-V* curves for $AuPt_{0.2}/GaN/n^+$-p Si (in CO_2-saturated 0.5 M $KHCO_3$ aqueous solution) and $NiFeO_x/BiVO_4$ photoanode (in 0.5 M KBi) in a three-electrode configuration. The photocathode data was plotted with the sign of the photocurrent inverted. Related to Figure 4.

Table S1 Contributions to the adsorbate free energy from the corrections of zero-point energy, heat capacity, and entropy, respectively. The assumed fugacity for each non-adsorbed species are also included. H_2 (ref) is used for the computational hydrogen electrode model as described in Computational Methods Section. Related to Figure 1.

Species	Fugacity (Pa)	ZPE (eV)	$\int C_p dT$ (eV)	-TS (eV)
*COOH	-	0.62	0.10	-0.27
*CO	-	0.19	0.08	-0.16
*H	-	0.16	0.01	-0.01
H_2 (ref)	101325	0.27	0.09	-0.42
CO	101325	0.14	0.09	-0.67
H_2O	3534	0.58	0.10	-0.65
CO_2	101325	0.31	0.10	-0.65

Table S2. ICP-AES analysis of Au and Pt loading amounts of different samples. Related to Figure 2.

Sample	Au/GaN/ n^+-p Si	AuPt$_{0.1}$/GaN/ n^+-p Si	AuPt$_{0.2}$/GaN/ n^+-p Si	AuPt$_{0.4}$/GaN/ n^+-p Si	Pt/GaN/ n^+-p Si
Au (nmol cm^{-2})	8.5	8.8	8.5	8.6	-
Pt (nmol cm^{-2})	-	0.9	1.7	3.4	3.7

Table S3. Performance comparison of photocathodes for PEC CO_2 reduction into CO/syngas at underpotential (more positive than the equilibrium potential $E^o(CO_2/CO) = -0.11$ V vs RHE). Related to Figure 3.

Photocathode	Light intensity (mW cm^{-2})	Onset potential (V vs RHE) [a]	FE$_{CO}$ (%)[b]	ABPE (%)[c]	Refs
Cu-ZnO/GaN/n$^+$-p Si	800	0.1	70	~0.01	Chu et al., 2016
Au$_3$Cu/n$^+$-p Si	20	0.15	80	0.07	Kong et al., 2016
Au/n$^+$-p Si	100	0.2	91	0.12	Song et al., 2017
Au/ZnO@ZnTe@CdTe	100	0.45	67	0.18	Jang et al., 2016
Ag$_2$P/Al$_2$O$_3$/n$^+$-p Si	100	0.3	67	0.3	Li et al., 2019
Au/TiO$_2$/a-Si	100	0.4	50	0.42	Li et al., 2019
Pt-TiO$_2$/GaN/n$^+$-p Si	800	0.5	78	0.87	Chu et al., 2018
Cu$_3$(BTC)$_2$/Cu$_2$O	100	-1.77 V vs Fc/Fc$^+$	95	0.83	Deng et al., 2019
AuPt/GaN/n$^+$-p Si	100	0.45	91	1.88	This work

[a] The potential reported at photocurrent density of 0.5 mA cm^{-2}.

[b] The highest FE reported in the system.

[c] Calculated using equation 7 in Methods Section.

Table S4. Performance comparison of recent state-of-the-art catalysts for (photo)electrochemical CO_2 reduction into CO. Related to Figure 3.

Catalytic architecture	Potential	TOF (h^{-1})	Refs.
Ag/Si NWs	-1.4 V *vs.* RHE	2400	Wei et al., 2019
Single Sb/NC	-0.9 V vs. RHE	16600	Jia et al., 2019
Single Ni/graphene	2.78 V vs. RHE	210000	Jiang et al., 2018
Ni^I-NCNT@Ni_9Cu	-0.73 V *vs.* RHE	1962	Zhang et al., 2020
NC-CNTs (Ni)	-1.0 V *vs.* RHE	11650	Fan et al., 2019
PyNiPc	-0.93 V vs. RHE	13000	Ma et al., 2020
Cr(^{tbu}dhbpy)Cl(H_2O)	-0.22 V vs. RHE	20520	Hooe et al., 2019
Fe-TPP-Dimer/CNT	-0.88 V vs. RHE	36000	Abdinejad et al., 2020
meta-Re(bpy)(CO)3Cl	-1.98 V vs. $Fc^{+/0}$	860400	Talukdar et al., 2020
AuPt/GaN/n^+-p Si	0.17 V *vs.* RHE	56400	This work

Reference:

Abdinejad, M., Dao, C., Deng, B., Sweeney, M.E., Dielmann, F., Zhang, X., and Kraatz, H.B. (2020). Enhanced electrochemical reduction of CO_2 to CO upon immobilization onto carbon nanotubes using an iron-porphyrin dimer. ChemistrySelect *5*, 979-984.

Blöchl, P. E. (1994) Projector augmented-wave method. Phys. Rev. B *50*, 17953.

Chu, S., Fan, S. Z., Wang, Y. J., Rossouw, D., Wang, Y. C., Botton, G. A., and Mi, Z. (2016) Tunable syngas production from CO_2 and H_2O in an aqueous photoelectrochemical cell. Angew. Chem. Int. Ed. *55*, 14260-14264.

Chu, S., Ou, P., Ghamari, P., Vanka, S., Zhou, B., Shih, I., Song, J., and Mi, Z. (2018) Photoelectrochemical CO_2 reduction into syngas with the metal/oxide interface. J. Am. Chem. Soc. *140*, 7869-7877.

Deng, X., Li, R., Wu, S., Wang, L., Hu, J., Ma, J., Jiang, W., Zhang, N., Zheng, X., Gao, C., Wang, L., Zhang, Q., Zhu, J., and Xiong, Y. (2019) Metal-organic framework coating enhances the performance of Cu_2O in photoelectrochemical CO_2 reduction. J. Am. Chem. Soc. *141*, 10924-10929.

Fan, Q., Hou, P., Choi, C., Wu, T.S., Hong, S., Li, F., Soo, Y.L., Kang, P., Jung, Y., and Sun, Z. (2019). Activation of Ni particles into single Ni–N atoms for efficient electrochemical reduction of CO_2. Adv. Energy Mater. *10,* 1903068.

Hooe, S.L., Dressel, J.M., Dickie, D.A., and Machan, C.W. (2019). Highly efficient electrocatalytic reduction of CO_2 to CO by a molecular chromium complex. ACS Catal.. *10*, 1146-1151.

Jang, Y. J., Jeong, I., Lee, J., Lee, J., Ko, M. J., Lee, J. S. Unbiased sunlight-driven artificial photosynthesis of carbon monoxide from CO_2 using a ZnTe-based photocathode and a perovskite solar cell in tandem. *ACS Nano* **2016,** *10*, 6980.

Jia, M., Hong, S., Wu, T.-S., Li, X., Soo, Y.-L., and Sun, Z. (2019). Single Sb sites for efficient electrochemical CO_2 reduction. Chem. Commun. *55*, 12024-12027.

Jiang, K., Siahrostami, S., Zheng, T., Hu, Y., Hwang, S., Stavitski, E., Peng, Y., Dynes, J., Gangisetty, M., Su, D*., et al.* (2018). Isolated Ni single atoms in graphene nanosheets for high-performance CO_2 reduction. Energy Environ. Sci. *11*, 893-903.

Kim, T.W., and Choi, K.S. (2014). Nanoporous $BiVO_4$ photoanodes with dual-layer oxygen evolution catalysts for solar water splitting. Science *343*, 990-994.

Kobayashi, H., Sato, N., Orita, M., Kuang, Y., Kaneko, H., Minegishi, T., Yamada, T., and Domen, K. (2018). Development of highly efficient $CuIn_{0.5}Ga_{0.5}Se_2$-based photocathode and application to overall solar driven water splitting. Energy Environ. Sci. *11*, 3003-3009.

Kong, Q., Kim, D., Liu, C., Yu, Y., Su, Y., Li, Y., and Yang, P. D. (2016) Directed assembly of nanoparticle catalysts on nanowire photoelectrodes for photoelectrochemical CO_2 reduction. Nano Lett. *16*, 5675-5680.

Kresse, G., and Furthmüller, J. (1996) Efficiency of ab-initio total energy calculations for metals and semiconductors using a plane-wave basis set. Comput. Mater. Sci. *6*, 15.

Kresse, G., and Hafner, J. (1994) Ab initio molecular-dynamics simulation of the liquid-metal–amorphous-semiconductor transition in germanium. Phys. Rev. B *49*, 14251.

Kresse, G., and Joubert, D. (1999) From ultrasoft pseudopotentials to the projector augmented-

wave method. Phys. Rev. B *59*, 1758.

Li, C. C., Wang, T., Liu, B., Chen, M. X., Li, A., Zhang, G., Du, M. Y., Wang, H., Liu, S. F., and Gong, J. L. (2019) Photoelectrochemical CO_2 reduction to adjustable syngas on grain-boundary-mediated a-Si/TiO_2/Au photocathodes with low onset potentials. Energy Environ. Sci. *12*, 923-928.

Li, H., Wen, P., Itanze, D. S., Hood, Z. D., Ma, X., Kim, M., Adhikari, S., Lu, C., Dun, C., Chi, M., et al. (2019) Colloidal silver diphosphide (AgP_2) nanocrystals as low overpotential catalysts for CO_2 reduction to tunable syngas. Nat. Commun. *10, 5724.*

Li, L., Mu, X., Liu, W., Kong, X., Fan, S., Mi, Z., and Li, C. (2014) Thermal non-oxidative aromatization of light alkanes catalyzed by gallium nitride. Angew. Chem. Int. Ed. *53*, 14106.

Ma, D.-D., Han, S.-G., Cao, C., Li, X., Wu, X.-T., and Zhu, Q.-L. (2020). Remarkable electrocatalytic CO_2 reduction with ultrahigh CO/H_2 ratio over single-molecularly immobilized pyrrolidinonyl nickel phthalocyanine. Appl. Catal. B *264, 118530.*

Monkhorst, H. J., and Pack, J. D. (1976) Special points for brillouin-zone integrations. Phys. Rev. B *13*, 5188.

Nørskov, J. K., Rossmeisl, J., Logadottir, A., Lindqvist, L., Kitchin, J. R., Bligaard, T., and Jonsson, H. (2004) Origin of the overpotential for oxygen reduction at a fuel-cell cathode. J. Phys. Chem. B *108*, 17886.

Sheng, W., Kattel, S., Yao, S., Yan, B., Liang, Z., Hawxhurst, C. J., Wu, Q., and Chen, J. G. (2017) Electrochemical reduction of CO_2 to synthesis gas with controlled CO/H_2 ratios. Energy Environ. Sci. *10*, 1180.

Song, J. T., Ryoo, H., Cho, M., Kim, J., Kim, J. G., Chung, S. Y., and Oh, J. (2017) Nanoporous Au Thin Films on Si Photoelectrodes for Selective and Efficient Photoelectrochemical CO_2 Reduction. Adv. Energy Mater. *7,* 1601103.

Sui, M., Li, M. Y., Kim, E. S., and Lee, J. (2013) Annealing temperature effect on self-assembled Au droplets on Si (111). Nanoscale Res. Lett. *8,* 525.

Talukdar, K., Sinha Roy, S., Amatya, E., Sleeper, E.A., Le Magueres, P., and Jurss, J.W. (2020). Enhanced electrochemical CO_2 Reduction by a series of molecular rhenium catalysts decorated with second-sphere hydrogen-bond donors. Inorg. Chem. *59,* 6087-6099.

Tripković, V., Skúlason, E., Siahrostami, S., Nørskov, J. K., and Rossmeisl, J. (2010) The oxygen reduction reaction mechanism on Pt(111) from density functional theory calculations. Electrochimi. Acta *55,* 7975.

Vanka, S., Arca, E., Cheng, S., Sun, K., Botton, G. A., Teeter, G., and Mi, Z. (2018) High efficiency Si photocathode protected by multifunctional GaN nanostructures. Nano Lett. *18,* 6530.

Wei, L., Lin, J., Xie, S., Ma, W., Zhang, Q., Shen, Z., and Wang, Y. (2019). Photoelectrocatalytic reduction of CO_2 to syngas over Ag nanoparticle modified p-Si nanowire arrays. Nanoscale *11,* 12530-12536.

Wellendorff, J., Lundgaard, K. T., Møgelhøj, A., Petzold, V., Landis, D. D., Nørskov, J. K., Bligaard, T., and Jacobsen, K. W. (2012) Density functionals for surface science: Exchange-correlation model development with bayesian error estimation. Phys. Rev. B *85,* 235149.

Zhang, T., Han, X., Yang, H., Han, A., Hu, E., Li, Y., Yang, X.q., Wang, L., Liu, J., and Liu, B. (2020). Atomically dispersed nickel(I) on an alloy-encapsulated nitrogen-doped carbon

nanotube array for high-performance electrochemical CO_2 reduction reaction. Angew. Chem. Int. Ed. doi.org/10.1002/anie.202002984.